Supporting Information

Hyperbolic metamaterial devices for wave-front manipulation

Xiang Yin[1,#], Hua Zhu[1,#], Huijie Guo[2], Ming Deng[1], Tao Xu[3], Zhijie Gong[4], Xun Li[1], Zhi Hong Hang[3], Chao Wu[4], Hongqiang Li[4], Shuqi Chen[5], Lei Zhou[2,], and Lin Chen[1,]**

[1]Wuhan National Laboratory for Optoelectronics, Huazhong University of Science and Technology, Wuhan 430074, China.

[2]State Key Laboratory of Surface Physics and Key Laboratory of Micro and Nano Photonic Structures (Ministry of Education), Fudan University, Shanghai 200433, China.

[3]College of Physics, Optoelectronics and Energy and Collaborative Innovation Center of Suzhou Nano Science and Technology, Soochow University, Suzhou 215006, China.

[4]School of Physics Science and Engineering, Shanghai Key Laboratory of Special Artificial Microstructure Materials and Technology, Tongji University, Shanghai 200092, China.

[5]The MOE Key Laboratory of Weak Light Nonlinear Photonics, School of Physics and TEDA Institute of Applied Physics, Nankai University, Tianjin 300071, China.

[#] These authors contributed equally to this work.

*Corresponding Author, email:
phzhou@fudan.edu.cn,
chen.lin@mail.hust.edu.cn

Note 1: Theoretical calculation of the dispersion relation of the SSP mode supported by an HMM waveguide (array)

A. One-dimensional HMM waveguide of finite width

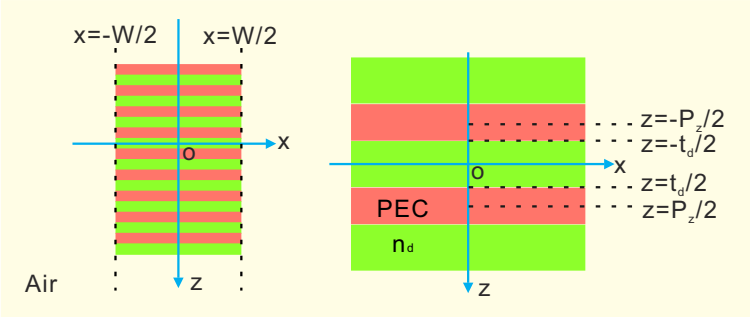

Figure S1. Schematic of one-dimensional HMM waveguide

In the microwave frequency domain, metal can be treated as perfect electric conductor. Assuming that the wavelength of light is much larger than the lattice constant along z direction ($t_d < P_z << \lambda_0$), all the high-order diffraction can be safely neglected except the first-order in $x < -W/2$ and $x > W/2$ regions. The electromagnetic (EM) fields for the transverse magnetic (TM) mode can be written as

$$E_z = \begin{cases} \rho_0 e^{ik_z z} e^{-ik_x x} / \sqrt{P_z} & (x < -W/2) \\ \rho_0' e^{ik_z z} e^{ik_x x} / \sqrt{P_z} & (x > W/2) \end{cases} \tag{S1}$$

$$H_y = \begin{cases} k_0 \rho_0 e^{ik_z z} e^{-ik_x x} / (k_x \sqrt{P_z}) & (x < -W/2) \\ -k_0 \rho_0' e^{ik_z z} e^{ik_x x} / (k_x \sqrt{P_z}) & (x > W/2) \end{cases} \tag{S2}$$

where $k_0 = \omega / c_0$ is the wavenumber in free space and k_z is the propagation constant along z direction, $k_x = \sqrt{k_0^2 - k_z^2}$, and $\rho_0 / \sqrt{P_z}$ and $\rho_0' / \sqrt{P_z}$ are the amplitudes of the electric field of E_z in the corresponding regions.

In the dielectric spacer regions ($|x| < W/2$), the fundamental TM mode will dominate since t_d is much smaller than the wavelength of radiation. Therefore, only the fundamental TM mode need to be considered in the modal expansion of the EM fields inside the dielectric layer

$$E_z = [C_+ e^{in_d k_0 x} + C_- e^{-in_d k_0 x}] / \sqrt{t_d}\,, \tag{S3}$$

$$H_y = [-n_d C_+ e^{in_d k_0 x} + n_d C_- e^{-in_d k_0 x}] / \sqrt{t_d}\,, \tag{S4}$$

where $C_+ / \sqrt{t_d}$ and $C_- / \sqrt{t_d}$ are the amplitude of the forward and backward propagating TM modes, respectively.

By connecting Equation S1-S4 with the Maxwell's boundary conditions that the tangential fields of E_z, and H_y must be continuous at $x = \pm W/2$, we can easily get the following equation set

$$\begin{cases} \rho_0 \varphi_+ = [C_+ \varphi_-' + C_- \varphi_+']S_0 \\ \rho_0' \varphi_+ = [C_+ \varphi_+' + C_- \varphi_-']S_0 \\ -\dfrac{k_0 S_0}{k_x} \rho_0 \varphi_+ = [C_+ \varphi_-' - C_- \varphi_+']n_d \\ \dfrac{k_0 S_0}{k_x} \rho_0' \varphi_+ = [C_+ \varphi_+' - C_- \varphi_-']n_d \end{cases} \tag{S5}$$

where $S_0 = \dfrac{1}{\sqrt{P_z t_d}} \int_{-P_z}^{P_z} e^{ik_z z} dz = \sqrt{\dfrac{t_d}{P_z}} \dfrac{\sin(k_z t_d / 2)}{k_z t_d / 2}$, $\varphi_+ = e^{ik_x W/2}$, and $\varphi_\pm' = e^{\pm in_d k_0 W/2}$. By eliminating C_+, and C_-, we can further get $e^{in_d k_0 W} = -\dfrac{A_+}{A_-}\dfrac{\rho_0'}{\rho_0} = -\dfrac{A_+}{A_-}\dfrac{\rho_0}{\rho_0'}$ and $\dfrac{\rho_0}{\rho_0'} = \pm 1$, where $A_\pm = \dfrac{k_0 S_0^2}{k_x} \pm n_d$:

(1) If $\rho_0 = \rho_0'$, then $\dfrac{k_0 S_0^2}{k_x} = in_d \tan(n_d k_0 W/2)$. Because the dispersion curve of the SSP mode must deviate more far from the light line, i.e. $k_z > k_0$, hence we have $k_x = i\sqrt{k_z^2 - k_0^2}$. We can thus obtain the dispersion relation as $\sqrt{k_z^2 - k_0^2} = -k_0 S_0^2 \cot(n_d k_0 W/2)/n_d$ for asymmetrical SSP mode.

(2) If $\rho_0 = -\rho_0'$, then $\dfrac{k_0 S_0^2}{k_x} = -in_d \cot(n_d k_0 W/2)$. We can obtain the dispersion relation as $\sqrt{k_z^2 - k_0^2} = k_0 S_0^2 \tan(n_d k_0 W/2)/n_d$ for symmetrical SSP mode by taking account into the relation of k_x and k_z as $k_x = \sqrt{k_0^2 - k_z^2}$.

B. One-dimensional HMM waveguide array

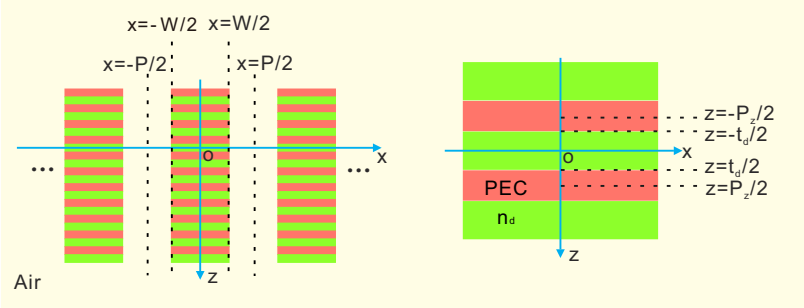

Figure S2. Schematic of one-dimensional HMM waveguide array.

Similar to Note 1A, we firstly write out the EM fields in all the regions except in the metal region:

$$E_z = \begin{cases} [\rho_+ e^{ik_z z} e^{ik_x x} + \rho_- e^{ik_z z} e^{-ik_x x}]/\sqrt{P_z} & (-P/2 < x < -W/2) \\ [\rho_+' e^{ik_z z} e^{ik_x x} + \rho_-' e^{ik_z z} e^{-ik_x x}]/\sqrt{P_z} & (W/2 < x < P/2) \end{cases} \tag{S6}$$

$$H_y = \begin{cases} k_0[-\rho_+ e^{ik_z z} e^{ik_x x} + \rho_- e^{ik_z z} e^{-ik_x x}]/(k_x\sqrt{P_z}) & (-P/2 < x < -W/2) \\ k_0[-\rho_+' e^{ik_z z} e^{ik_x x} + \rho_-' e^{ik_z z} e^{-ik_x x}]/(k_x\sqrt{P_z}) & (W/2 < x < P/2) \end{cases} \tag{S7}$$

$$E_z = \begin{cases} [C_+ e^{in_d k_0 x} + C_- e^{-in_d k_0 x}]/\sqrt{t_d} & (-t_d/2 < z < t_d/2, |x| < W/2) \\ 0 & (t_d/2 < |z| < P_z/2, |x| < W/2) \end{cases} \tag{S8}$$

$$H_y = [-n_d C_+ e^{in_d k_0 x} + n_d C_- e^{-in_d k_0 x}]/\sqrt{t_d} \quad (-t_d/2 < z < t_d/2, |x| < W/2) \tag{S9}$$

where $\rho_\pm$, $\rho_\pm'$ and $C_\pm$ are unsolved coefficients related to mode amplitudes in different regions.

One can connect Equation S6-S9 with the Maxwell's boundary conditions and the periodic boundary conditions, yielding the following relations

$$\begin{cases} \rho_+\varphi_- + \rho_-\varphi_+ = (C_+\varphi_-' + C_-\varphi_+')S_0 & (E_z, x = -W/2) \\ \rho_+'\varphi_+ + \rho_-'\varphi_- = (C_+\varphi_+' + C_-\varphi_-')S_0 & (E_z, x = W/2) \\ \rho_+\varphi_- S_0 k_0/k_x - \rho_-\varphi_+ S_0 k_0/k_x = (C_+\varphi_-' - C_-\varphi_+')n_d & (H_y, x = -W/2) \\ \rho_+'\varphi_+ S_0 k_0/k_x - \rho_-'\varphi_- S_0 k_0/k_x = (C_+\varphi_+' - C_-\varphi_-')n_d & (H_y, x = W/2) \\ \rho_+\varphi_-^P + \rho_-\varphi_+^P = \rho_+'\varphi_+^P + \rho_-'\varphi_-^P & (E_z, |x| = P/2) \\ \rho_+\varphi_-^P - \rho_-\varphi_+^P = \rho_+'\varphi_+^P - \rho_-'\varphi_-^P & (H_y, |x| = P/2) \end{cases} \tag{S10}$$

where $\varphi_\pm = e^{\pm ik_x W/2}$, $\varphi_\pm' = e^{\pm in_d k_0 W/2}$, $\varphi_\pm^P = e^{\pm ik_x P/2}$ and $S_0 = \sqrt{\frac{t_d}{P_z}}\frac{\sin(k_z t_d/2)}{k_z t_d/2}$.

By eliminating $\rho_{\pm}$, $\rho_{\pm}'$ and $C_{\pm}$ in Equation S10, we obtain

$$\pm A_{-}[\tan(\frac{n_d k_0 W}{2}) - \tan(\frac{k_x g}{2})] = A_{+}[\tan(\frac{n_d k_0 W}{2}) + \tan(\frac{k_x g}{2})] \quad \text{(S11)}$$

where $g = P - W$ and $A_{\pm} = \frac{k_0 S_0^2}{k_x} \pm n_d$:

(1) If $A_{-}[\tan(\frac{n_d k_0 W}{2}) - \tan(\frac{k_x g}{2})] = A_{+}[\tan(\frac{n_d k_0 W}{2}) + \tan(\frac{k_x g}{2})]$, then $-n_d \tan(\frac{n_d k_0 W}{2}) = \frac{k_0}{k_x} S_0^2 \tan(\frac{k_x g}{2})$. By using $k_x = i\sqrt{k_z^2 - k_0^2}$, the dispersion relation can be expressed as

$$\sqrt{k_z^2 - k_0^2} = -k_0 S_0^2 \frac{1 - e^{-\sqrt{k_z^2 - k_0^2} g}}{1 + e^{-\sqrt{k_z^2 - k_0^2} g}} \cot(\frac{n_d k_0 W}{2}) / n_d \quad \text{(S12)}$$

for asymmetrical SSP mode. As $g \to +\infty$, $\frac{1 - e^{-\sqrt{k_z^2 - k_0^2} g}}{1 + e^{-\sqrt{k_z^2 - k_0^2} g}} \to 1$, Equation S12 will be reduced to the dispersion relation for the asymmetrical SSP mode in Note 1A.

(2) If $-A_{-}[\tan(\frac{n_d k_0 W}{2}) - \tan(\frac{k_x g}{2})] = A_{+}[\tan(\frac{n_d k_0 W}{2}) + \tan(\frac{k_x g}{2})]$, then $-n_d \tan(\frac{k_x g}{2}) = \frac{k_0}{k_x} S_0^2 \tan(\frac{n_d k_0 W}{2})$. By using $k_x = i\sqrt{k_z^2 - k_0^2}$, we can get

$$\sqrt{k_z^2 - k_0^2} = k_0 S_0^2 \frac{1 + e^{-\sqrt{k_z^2 - k_0^2} g}}{1 - e^{-\sqrt{k_z^2 - k_0^2} g}} \tan(\frac{n_d k_0 W}{2}) / n_d \quad \text{(S13)}$$

for symmetrical SSP mode. As $g \to +\infty$, $\frac{1 - e^{-\sqrt{k_z^2 - k_0^2} g}}{1 + e^{-\sqrt{k_z^2 - k_0^2} g}} \to 1$, Equation S13 will be reduced to the dispersion relation for the symmetrical SSP mode in Note 1A.

Note 2: Theoretical calculation of the complex reflection/transmission coefficients for one-dimensional HMM waveguide array

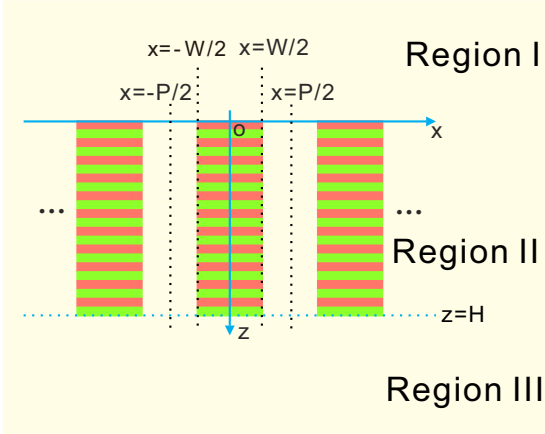

Figure S3. Schematic of one-dimensional HMM waveguide array.

For one-dimensional HMM waveguide array with a finite height of H, normally illuminated with x-polarized plane-waves, the EM fields in region I (z<0) and region III (z>H) can be written as [A1]

$$\begin{cases} H_y^I = e^{ik_0 z} + \sum_{n=-\infty}^{+\infty} r_n e^{ik_{x,air}^{(n)} x} e^{-ik_{z,air}^{(n)} z} \\ E_x^I = k_0 e^{ik_0 z} - \sum_{n=-\infty}^{+\infty} r_n k_{z,air}^{(n)} e^{ik_{x,air}^{(n)} x} e^{-ik_{z,air}^{(n)} z} \\ H_y^{III} = \sum_{n=-\infty}^{+\infty} t_n e^{ik_{x,air}^{(n)} x} e^{ik_{z,air}^{(n)} (z-H)} \\ E_x^{III} = \sum_{n=-\infty}^{+\infty} t_n k_{z,air}^{(n)} e^{ik_{x,air}^{(n)} x} e^{ik_{z,air}^{(n)} (z-H)} \end{cases} \tag{S14}$$

where $k_{x,air}^{(n)} = 2n\pi / P$, $k_{z,air}^{(n)} = \sqrt{k_0^2 - (k_{x,air}^{(n)})^2}$, r_n / t_n is the complex reflection/transmission coefficient with the diffraction order of n .

In region II (0<z<H), the EM fields can be expressed as a linear combination of all the symmetric modes

$$\begin{cases} H_y^{II} = \sum_{m=1}^{+\infty} 2\cos[k_{x,HMM}^{(m)}(x+P/2)][B_+^{(m)} e^{ik_{z,HMM}^{(m)} z} + B_-^{(m)} e^{ik_{z,HMM}^{(m)}(H-z)}](-P/2 < x < -W/2) \\ E_x^{II} = \sum_{m=1}^{+\infty} 2k_{z,HMM}^{(m)} \cos[k_{x,HMM}^{(m)}(x+P/2)][B_+^{(m)} e^{ik_{z,HMM}^{(m)} z} - B_-^{(m)} e^{ik_{z,HMM}^{(m)}(H-z)}](-P/2 < x < -W/2) \\ H_y^{II} = \sum_{m=1}^{+\infty} 2\cos[k_{x,HMM}^{(m)}(x-P/2)][B_+^{(m)} e^{ik_{z,HMM}^{(m)} z} + B_-^{(m)} e^{ik_{z,HMM}^{(m)}(H-z)}](W/2 < x < P/2) \\ E_x^{II} = \sum_{m=1}^{+\infty} 2k_{z,HMM}^{(m)} \cos[k_{x,HMM}^{(m)}(x-P/2)][B_+^{(m)} e^{ik_{z,HMM}^{(m)} z} - B_-^{(m)} e^{ik_{z,HMM}^{(m)}(H-z)}](W/2 < x < P/2) \end{cases} \tag{S15}$$

By connecting Equations S14-S15 with the Maxwell's boundary conditions, we can yield the following equation set as

$$\begin{cases} \sum_{n=-\infty}^{+\infty}(\delta_{n0}+r_n)S_z^{(n,m)} = I_m(B_+^{(m)}+B_-^{(m)}e^{ik_{z,HMM}^{(m)}H}) \\ \sum_{n=-\infty}^{+\infty} t_n S_z^{(n,m)} = I_m(B_+^{(m)}e^{ik_{z,HMM}^{(m)}H}+B_-^{(m)}) \\ k_{z,air}^{(n)}(\delta_{n0}-r_n)P/g = \sum_{m=1}^{+\infty}(B_+^{(m)}-B_-^{(m)}e^{ik_{z,HMM}^{(m)}H})k_{z,HMM}^{(m)}S_z^{(n,m)} \\ k_{z,air}^{(n)}t_n P/g = \sum_{m=1}^{+\infty}(B_+^{(m)}e^{ik_{z,HMM}^{(m)}H}-B_-^{(m)})k_{z,HMM}^{(m)}S_z^{(n,m)} \end{cases} \tag{S16}$$

where $S_z^{(n,m)} = 2\{\int_{-P/2}^{-W/2} e^{ik_{x,air}^{(n)}x}\cos[k_{x,HMM}^{(m)}(x+P/2)]dx + \int_{W/2}^{P/2} e^{ik_{x,air}^{(n)}x}\cos[k_{x,HMM}^{(m)}(x-P/2)]dx\}/g =$

$(-1)^n\{\frac{\sin[(k_{x,HMM}^{(m)}+k_{x,air}^{(n)})g/2]}{(k_{x,HMM}^{(m)}+k_{x,air}^{(n)})g/2} + \frac{\sin[(k_{x,HMM}^{(m)}-k_{x,air}^{(n)})g/2]}{(k_{x,HMM}^{(m)}-k_{x,air}^{(n)})g/2}\}$,

$I_m = 4\{\int_{-P/2}^{-W/2}\cos^2[k_{x,HMM}^{(m)}(x+P/2)]dx + \int_{W/2}^{P/2}\cos^2[k_{x,HMM}^{(m)}(x-P/2)]dx\}/g = 2+\frac{2\sin(k_{x,HMM}^{(m)}g)}{k_{x,HMM}^{(m)}g}$.

By eliminating r_n and t_n in Equation S16, $B_+^{(m)}$ and $B_-^{(m)}$ can be expressed as

$$\begin{cases} 2S_z^{(0,m)} = \sum_{n=-\infty}^{+\infty}\sum_{l=1}^{+\infty}\frac{k_{z,HMM}^{(l)}S_z^{(n,m)}S_z^{(n,l)}g}{k_{z,air}^{(n)}P}(B_+^{(l)}-B_-^{(l)}e^{ik_{z,HMM}^{(l)}H}) + I_m(B_+^{(m)}+B_-^{(m)}e^{ik_{z,HMM}^{(m)}H}) \\ 0 = \sum_{n=-\infty}^{+\infty}\sum_{l=1}^{+\infty}\frac{k_{z,HMM}^{(l)}S_z^{(n,m)}S_z^{(n,l)}g}{k_{z,air}^{(n)}P}(B_+^{(l)}e^{ik_{z,HMM}^{(l)}H}-B_-^{(l)}) - I_m(B_+^{(m)}e^{ik_{z,HMM}^{(m)}H}+B_-^{(m)}) \end{cases} \tag{S17}$$

Then r_n and t_n can be rewritten with a combination of $B_+^{(m)}$ and $B_-^{(m)}$

$$\begin{cases} r_n = \delta_{n0} - \frac{g}{P}\sum_{m=1}^{+\infty}\frac{k_{z,HMM}^{(m)}}{k_{z,air}^{(n)}}(B_+^{(m)}-B_-^{(m)}e^{ik_{z,HMM}^{(m)}H})S_z^{(n,m)} \\ t_n = \frac{g}{P}\sum_{m=1}^{+\infty}\frac{k_{z,HMM}^{(m)}}{k_{z,air}^{(n)}}(B_+^{(m)}e^{ik_{z,HMM}^{(m)}H}-B_-^{(m)})S_z^{(n,m)} \end{cases} \tag{S18}$$

The reflection/transmission (R/T) efficiency can thus be expressed as [A2]

$$\begin{cases} R = \sum_{n=-\infty}^{+\infty}|r_n|^2\, real(k_{z,air}^{(n)}/k_0) \\ T = \sum_{n=-\infty}^{+\infty}|t_n|^2\, real(k_{z,air}^{(n)}/k_0) \end{cases} \tag{S19}$$

The coupling efficiency between the n-order diffracted waves in the air and the m-th symmetric mode supported by the HMM waveguide array can be retrieved as

$$\eta^{(n,m)}=\frac{[\int_{-P/2}^{P/2}E_{x,air}^{(n)}E_{x,HMM}^{(m)*}dx]^2}{\int_{-P/2}^{P/2}E_{x,air}^{(n)}E_{x,air}^{(n)*}dx\int_{-P/2}^{P/2}E_{x,HMM}^{(m)}E_{x,HMM}^{(m)*}dx}=\frac{g(S_z^{(n,m)})^2}{PI_m} \tag{S20}$$

For the HMM waveguide used in our work, only one guided SSP mode (m=0) is supported. By setting m=0 and neglecting the other leaky modes in Equation S17-S18, r_n and t_n can be rewritten as

$$\begin{cases} r_n=\delta_{n0}-2\dfrac{g}{P}\dfrac{k_{z,HMM}^{(0)}}{k_{z,air}^{(n)}}\dfrac{I_0-iM\tan(k_{z,HMM}^{(0)}H)}{2I_0M-i(M^2+I_0^2)\tan(k_{z,HMM}^{(0)}H)}S_z^{(n,0)}S_z^{(0,0)} \\ t_n=2\dfrac{g}{P}\dfrac{k_{z,HMM}^{(0)}}{k_{z,air}^{(n)}}\dfrac{I_0}{2I_0M\cos(k_{z,HMM}^{(0)}H)-i(M^2+I_0^2)\sin(k_{z,HMM}^{(0)}H)}S_z^{(n,0)}S_z^{(0,0)} \end{cases} \tag{S21}$$

where $M=\sum_{n=-\infty}^{+\infty}\dfrac{k_{z,HMM}^{(0)}(S_z^{(n,0)})^2g}{k_{z,air}^{(n)}P}$. Noting that $P<<\lambda$, then the 0-order complex reflection/transmission coefficient is

$$\begin{cases} r_0=1-2\dfrac{g}{P}\dfrac{k_{z,HMM}^{(0)}[I_0-iM\tan(k_{z,HMM}^{(0)}H)](S_z^{(0,0)})^2}{k_0[2I_0M-i(M^2+I_0^2)\tan(k_{z,HMM}^{(0)}H)]} \\ \quad=1-\dfrac{2\xi^{(0,0)}[1-i\sum_{n=-\infty}^{+\infty}\xi^{(0,0)}\tan(k_{z,HMM}^{(0)}H)]}{2\sum_{n=-\infty}^{+\infty}\xi^{(n,0)}-i[1+(\sum_{n=-\infty}^{+\infty}\xi^{(n,0)})^2]\tan(k_{z,HMM}^{(0)}H)} \\ t_0=2\dfrac{g}{P}\dfrac{k_{z,HMM}^{(0)}I_0(S_z^{(0,0)})^2}{k_0[2I_0M\cos(k_{z,HMM}^{(0)}H)-i(M^2+I_0^2)\sin(k_{z,HMM}^{(0)}H)]} \\ =\dfrac{2\xi^{(0,0)}}{2\sum_{n=-\infty}^{+\infty}\xi^{(n,0)}\cos(k_{z,HMM}^{(0)}H)-i[1+(\sum_{n=-\infty}^{+\infty}\xi^{(n,0)})^2]\sin(k_{z,HMM}^{(0)}H)} \end{cases} \tag{S22}$$

and the total transmission/reflection efficiency is

$$\begin{cases} T=|t_0|^2 \\ =\dfrac{4(\xi^{(0,0)})^2}{\{[(\xi^{(0,0)})^2-4(\sum_{n=1}^{+\infty}\xi^{(n,0)})^2-1]\sin(k_{z,HMM}^{(0)}H)-4i(\sum_{n=1}^{+\infty}\xi^{(n,0)})\cos(k_{z,HMM}^{(0)}H)\}^2+4(\xi^{(0,0)})^2} \\ R=1-T \end{cases} \tag{S23}$$

in which $\xi^{(n,m)}=\dfrac{k_{z,HMM}^{(m)}}{k_{z,air}^{(n)}}\eta^{(n,m)}$.

As W is close to zero, $\begin{cases} k_{z,HMM}^{(0)} \to k_0 \\ \eta^{(0,0)} \to 1 \\ \eta^{(n\neq 0,0)} \to 0 \end{cases}$, $\begin{cases} \xi^{(0,0)} \to 1 \\ \sum_{n=1}^{+\infty} \xi^{(n,0)} \to 0 \end{cases}$, we can get a nearly 100% transmission efficiency, T, for the incident EM waves.

Note 3: Overlap between the incident EM waves and asymmetric HMM waveguide mode

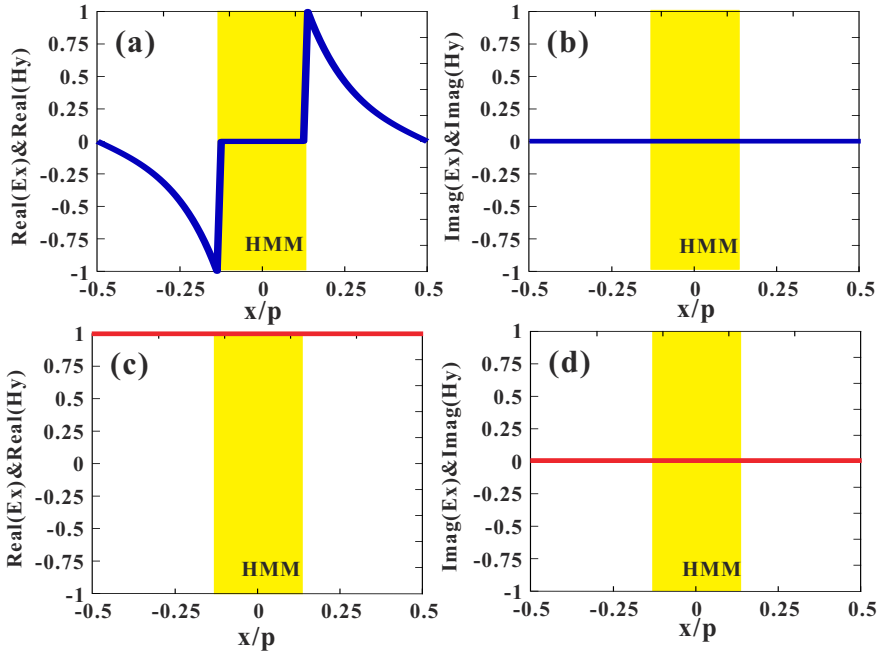

Figure S4. The normalized field distributions of real parts (a, c) and imaginary parts (b, d) of Ex and Hy of the asymmetric SSP mode of the HMM waveguide (a, b) and incident plane waves (c, d).

Power coupling efficiency represents the amount of power that can be coupled from one mode into a forward propagating wave with a different mode profile. The remaining power will be coupled into the backward propagating mode. Therefore, the power coupling efficiency is always less than or equal to the overlap between the two mode profiles [A3]. The overlap of the two modes (mode 1 and mode 2) can be extracted as

$$\text{overlap} = \frac{\left|\int_{-P/2}^{P/2} E_x^{(1)} H_y^{(2)*} dx\right| \left|\int_{-P/2}^{P/2} E_x^{(2)} H_y^{(1)*} dx\right|}{\int_{-P/2}^{P/2} E_x^{(1)} H_y^{(1)*} dx \int_{-P/2}^{P/2} E_x^{(2)} H_y^{(2)*} dx} \tag{S24}$$

The field distributions of the incident EM waves and asymmetric mode of the HMM waveguide are shown in Figure S4. It is apparent that the field distributions of the incident EM waves and asymmetric

mode are even and odd functions, respectively. Hence, both of $\left|\int_{-P/2}^{P/2} E_x^{(1)} H_y^{(2)*} dx\right|$ and $\left|\int_{-P/2}^{P/2} E_x^{(2)} H_y^{(1)*} dx\right|$ should be zero, namely, the overlap between the incident EM waves and asymmetric mode is zero. As a result, the power coupling efficiency between the incident EM waves and asymmetric mode should be zero.

Note 4: The role of high-order diffractions

As schematically shown in Figure S5 (a), when an incident plane wave normally illuminates the HMM waveguide array, the incident EM wave will be reflected to different diffraction orders in region I and coupled to all allowed modes (here, only the zero-order SSP mode is considered) in region II. Although the high-order diffracted waves are evanescent waves and can not reach the far-field, their presences are crucial to make the boundary conditions at the air/HMM interface satisfied, and thus they can indirectly modify the final strength of the SSP mode (zero-order) in region II. Furthermore, as the SSP mode in region II reaches the bottom boundary of the HMM waveguide, it not only can couple to the zero-order diffracted waves in region III but also can couple to all high-order diffracted waves in region III. Again, those high-order diffracted waves are of evanescent nature which can not reach the far-field directly, but their presences are essential to make the boundary conditions satisfied and they thus contribute indirectly to the transmission [Figure S5 (b)]. Finally, we note that the complicated multiple scatterings inside the HMM can involve all high-order modes in different regions, which, in turn, affect the final transmission characteristics of the whole device. Figure S5 (b) schematically presents the looping process mentioned above. As shown in Figure 1(g) in the main text, the transmission mainly comes from zero-order coupling from incident waves to SSP mode, $\eta^{(0,0)}$, as the width of the HMM waveguide is very small. As the width of the HMM waveguide is increased, the coupling from the high-order diffractions and SSP mode, $\eta^{(n,0)}$, increases, and hence makes extra contributions to the transmission efficiency.

Therefore, we can still realize high transmission efficiency even if the width of the HMM waveguide is very large [Figure 1(h) in the main text].

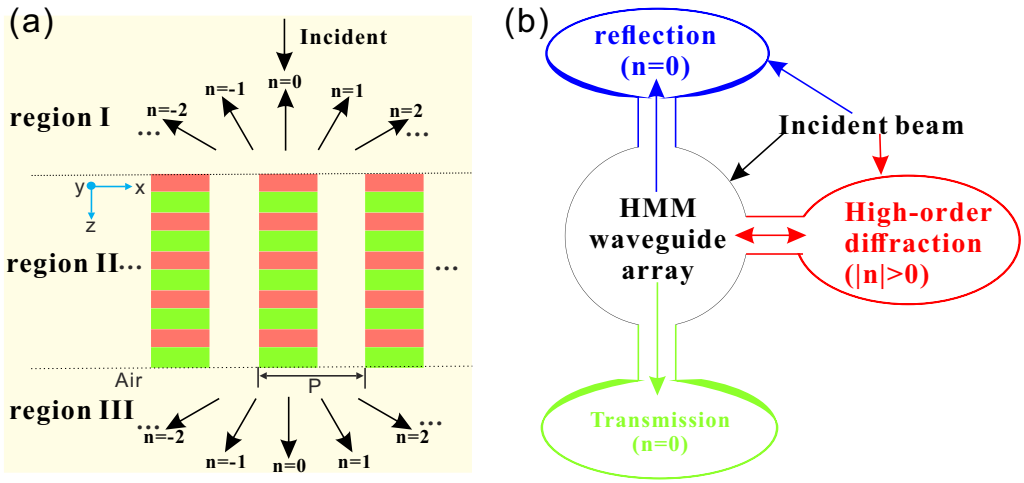

Figure S5. (a) Illustration of the plane waves illuminating the HMM waveguide array. (b) Schematic of the energy transport process of the incident beam and different diffraction orders.

Note 5: The effective refractive index and transmission of the HMM waveguide array

As an illustration, we calculated the effective refractive index of the SSP mode in the 1D-HMM waveguide array shown in Figure 1(d). As can be inferred from Figure 1(e) in the main text, the effective refractive index of the HMM waveguide firstly increases moderately, and increases sharply as the HMM waveguide width approaches the cut-off width. As shown in Figure S6 (a), the effective refractive index increases by 1.4 (from 1 to 2.4) when the width of HMM waveguide ranges from 0 to 5 mm. However, when the width of the HMM waveguide of the HMM waveguide increases from 5 mm to 6 mm, the effective refractive index increases by a large value of 9.7 (from 2.4 to 12.1). Correspondingly, the transmission efficiency for a HMM waveguide with a large width can be significantly reduced, compared with a HMM waveguide with a small width.

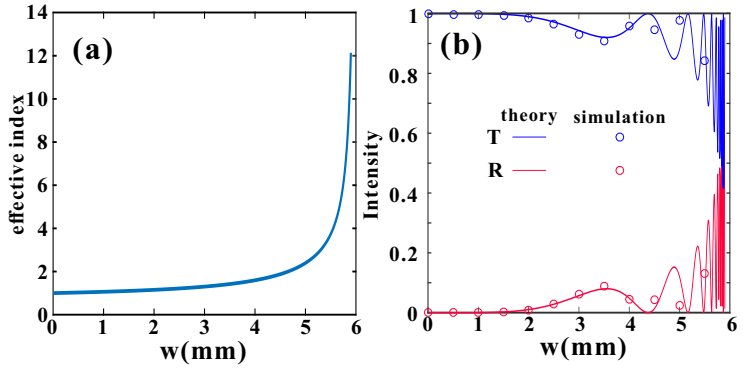

Figure S6. (a) Effective refractive index and (b) reflection/transmission intensity of the HMM waveguide array versus the width of the HMM waveguide at 12 GHz.

Note 6: Fabrication and measurement of beam deflectors and lenses

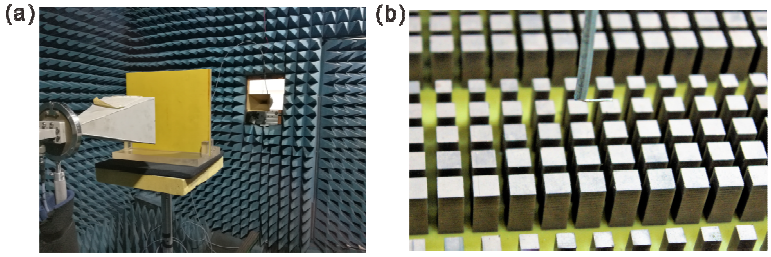

Figure S7. Experimental setup for (a) far-field and (b) near-field measurement.

The HMM is comprised of multilayered alternating Cu/FR4 layers. Each copper layer is printed on a FR4 layer through the multilayered printed circuit board. The Cu/FR4 composite layers are then adhered together by use of a 0.05 mm thick melt FR4, which ensures the uniformity for each dielectric spacer between the adjacent copper layers. Finally, a standard mechanical milling technique with computerized numerical control milling machine is used to form the desired pattern of the HMM waveguide arrays after the multi-layers on a thin FR4 substrate is ready.

The experimental setup for far-field and near-field measurement is presented in Figure S4. In the near-field measurement, a monopole antenna is used to probe the electric field [Figure S7b]. Far-field measurement and near-field scanning experiments are performed to characterize the device performances of the samples. In the far-field measurement, a horn antenna is used to receive the EM waves in the far-field. The receiving antenna can be flexibly rotated with respect to the samples to receive the angular spectrum. A reference measurement is implemented in the absence of the samples in the measuring zone. The far-field signals are normalized to the reference signals. Both the antennas are connected to a vector network analyzer (Agilent N5242A PNA-X). In the near-field scanning

experiments, the incident EM waves are generated by a horn antenna 2 m away from the samples. A monopole antenna in the output space is used to detect the electric field. The measured resolution is set to be 5 mm per step both along x, and z directions. Vector network analyzer (Keysight E5071C) is used for data acquisition.

Note 7: Simulated and measured near-field electric field distrubutions of the polarization-dependent beam deflector

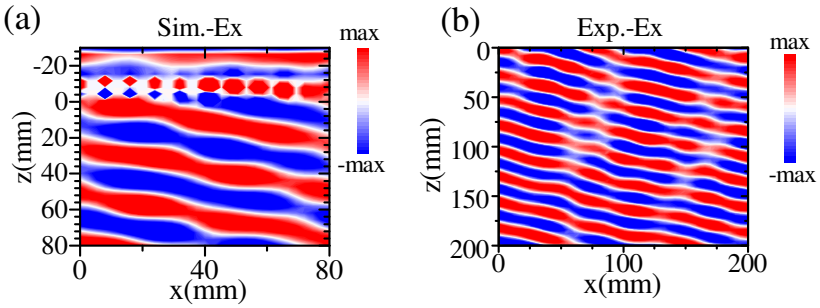

Figure S8. (a) Simulated and (b) measured near-field electric field distributions of E_x for the polarization-dependent beam deflector, illuminated with x-polarized plane-waves of normal incidence at 12 GHz.

Note 8: Design of the polarization-independent beam deflector

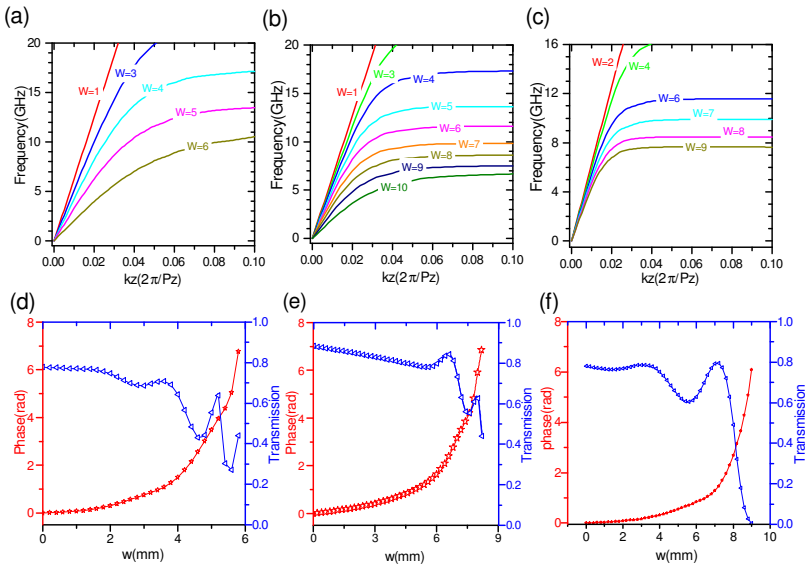

Figure S9. (a-c) The dispersion relation of x- (or y-) polarization for the SHMM waveguide array with the sub-unit period, *P*, of 6.6 (a), 11 (b), and 16.5 (c) mm for different waveguide width, *W*. (d-f) The transmission intensity and phase shift of x- (or y-) polarization as a function of the waveguide width, *W*, when the working frequency is 8 GHz.

In the design of the polarization-independent beam deflector, three structural parameters [height, *H*, period, *P*, and width, *W*] of the SHMM waveguide array should be considered. For

simplicity, the height of the SHMM waveguide is fixed at H =16.4 mm in the design, corresponding to 35 pair of Cu/FR4 layers. We have investigated a number of SHMM waveguide arrays with different sub-unit periods, and have come to the conclusion that 0-2π phase coverage could be more easily fulfilled if the sub-unit period of the SHMM waveguide array is sufficiently small. Here as an example, we have compared the phase coverage with three groups of sub-unit periods (6.6, 11, and 16.5 mm). The dispersion curves for different periods shown in Figure S9a-c indicate that the minimum period (P=6.6 mm) subjects to the largest variation range in the propagation constant when the waveguide width is varied within the same range. In other words, the full phase coverage 0-2π can be fulfilled with the minimum variation range for the waveguide width in the case of P =6.6 mm [Figure S9d-f]. Moreover, 0-2π phase coverage could not be provided at 8 GHz with the sub-unit period of 16.5 mm even if a sufficiently large waveguide width is used so that the working frequency approaches the cut-off frequency of the SSP mode [Figure S9f], which possibly fails to reshape the wave-front. We have presented the far-field intensity profiles of the designed beam deflector with P=6.6 mm [see the simulated results in Figure S10] and P=11 mm [see the simulated and measured results in Figure 4 in the main text].

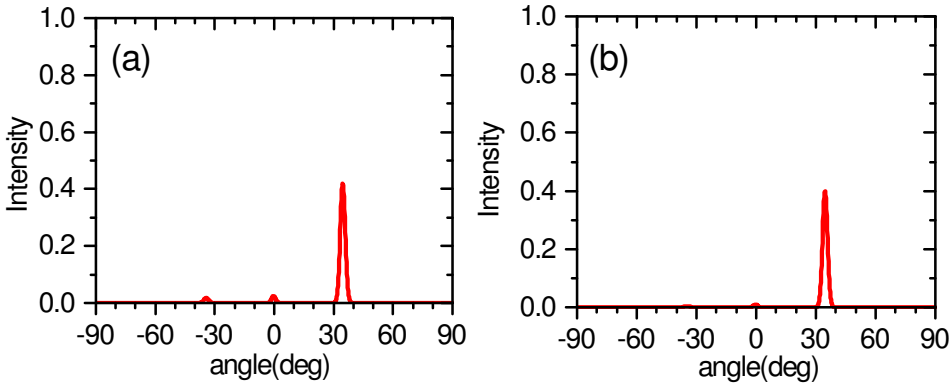

Figure S10. The simulated far-field intensity profiles for x- (a), and y- (b) polarized incident EM waves under normal incidence with the sub-unit period, P, of 6.6 mm. The waveguide widths for the sub-units within a super-cell are set to be 0, 0, 4.0, 4.0, 4.6, 4.6, 5.1, 5.1, 5.9, and 5.9 mm.

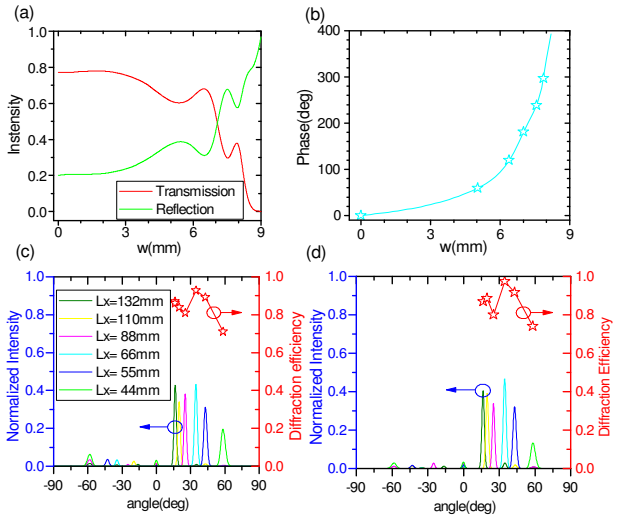

Figure S11. (a) The transmission, and reflection intensity versus the SHMM waveguide width, W, at 8 GHz. (b) The phase shift of the transmitted EM waves varies with W at 8 GHz. (c, d) The far-field electric field profiles and anomalous diffraction efficiency with different lattice constants (L_x) for x- (c), and y-polarized (d) incidences, respectively.

The transmission-intensity and transmission-phase as a function of the waveguide width are shown in Figure S11a,b, respectively. By using different number of the SHMM waveguide arrays within a supercell to cover 0-2π phase, we are able to achieve different anomalous refraction angles [Figure S11c,d]. All the transmitted EM waves are deflected along the desired angles, predicted by the general Snell's law [A4]. Note that, the diffraction efficiency can be more than 80% with L_x >44 mm. We have chosen L_x =66 mm to implement the experiment [see the fabricated sample in Figure 4 in the main text]. The simulated diffraction efficiencies for x- and y-polarizations can be as large as 92.7% and 97%, respectively.

Note 9: Simulated and measured near-field electric field distrubutions of the polarization-independent beam deflector

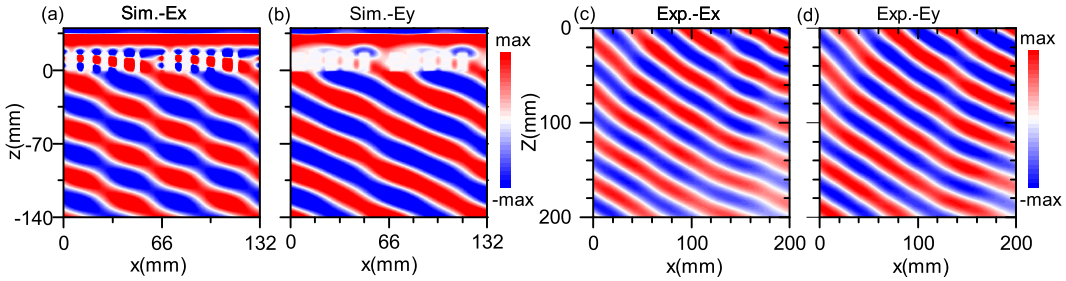

Figure S12. The simulated (a, b), and measured (c, d) electric field distributions of E_x and E_y in the output space for x-polarized incidence (a, c), and y-polarized incidence (b, d), respectively.

Note 10: Design of the polarization-independent focusing lens

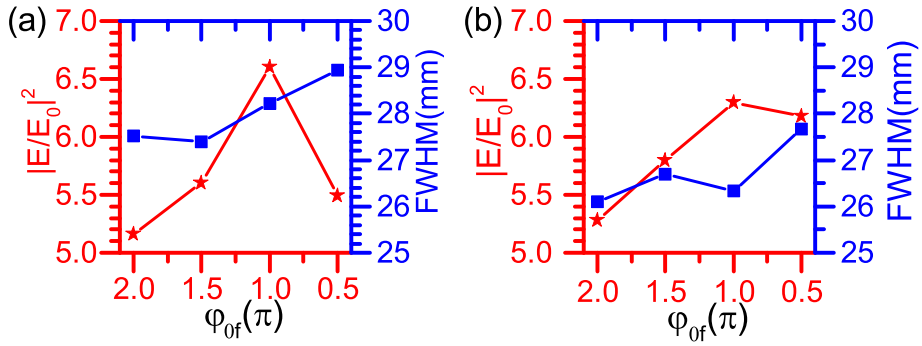

Figure S13. (a-b) The field intensity enhancement and the full width of half magnitude (FWHM) versus φ_{0f} for x- (a), and y- (b) polarized incidences, respectively.

In the design of the focusing lens, the spatial phase distributions should satisfy hyperboloidal profile as described by Equation 5 in the main text, which requires the phase shift φ_f decreases from the center to the side of the lens. With regard to the phase coverage presented in Figure S11b, one may directly place the sub-unit structures with the largest width in the center of the focusing lens, while arranging those sub-unit structures with the smaller width on both sides. However, the resultant phase distributions are accompanied with the minimum intensity transmission in the center of the focusing lens, which will somewhat weaken the focusing effect at the focal plane. As a result, we have optimized φ_{0f} to maximize the focusing intensity [see the focusing performance with different φ_{0f} in Figure S13]. The best focusing performance occurs at $\varphi_{0f}=\pi$, both for x- and y-polarized incidences, and the corresponding structural parameters have been used to implement the focusing experiment in the main text.

Note 11: Design of the half-wave plate with arrays of the RHMM waveguides

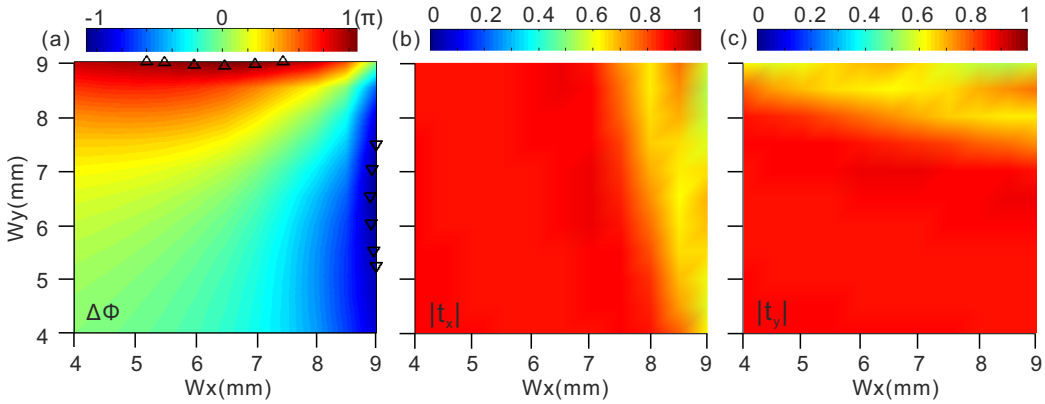

Figure S14. (a) The phase difference ($\Delta\varphi = \varphi_y - \varphi_x$) between the transmitted electric field of E_x, and E_y, and transmission amplitude for (b) x-, and (c) y-polarizations versus W_x, and W_y. The RHMM waveguide array is illuminated with x- and y-polarized EM waves at 7.6 GHz. The triangular symbols in (a) denote π phase difference. Other geometrical parameters are set as $P_x = P_y$ =13 mm, and $H = 35(t_m + t_d)$ (t_m =0.068 mm, t_d =0.47 mm).

As has been stated in the Section of operating principle in the main text, a complete polarization conversion for CP EM waves occurs as the complex transmission coefficients for the orthogonal polarizations satisfy $t_x + t_y = 0$. The phase difference ($\Delta\varphi = \varphi_y - \varphi_x$), and the transmission amplitude are calculated with FDTD simulations by sweeping the width (W_x , W_y) of the RHMM waveguide [Figure S14]. The selection criterion of (W_x , W_y) is π phase difference as well as minimum difference between the transmission amplitudes for x- and y-polarizations. Considering the calculation results presented in Figure S14, (W_x , W_y) is set to be (6 mm, 9 mm) for the design of a half-wave plate.

We next take two methods (FDTD simulation, and Effective-medium model) to analyze the performance of the RHMM waveguide array with W_x =6 mm, and W_y =9 mm. For the effective-medium method, the effective permittivity (ε), and permeability (μ) of the HMM can be expressed with a diagonal tensor form as

$$\varepsilon = \begin{pmatrix} PEC & & \\ & PEC & \\ & & \varepsilon_{zz} \end{pmatrix} \tag{S25}$$

$$\mu = \begin{pmatrix} \mu_{xx} & & \\ & \mu_{yy} & \\ & & 1 \end{pmatrix} \tag{S26}$$

where PEC stands for perfect electric conductor, ε_{zz}, and μ_{xx} ($\mu_{xx}=\mu_{yy}$) are presented in Figure S15. The phase difference, $\Delta\varphi$, as a function of frequency is plotted in Figure S16a. The calculated results by the two methods are basically consistent in the frequency range considered. We attribute the oscillations in the curves of transmission amplitude to Fabry-Perot cavity effect, originating from the reflection at the interface [Figure S16b]. Both methods reveal that $\Delta\varphi$ reaches approximately π at 7.6 GHz. As circularly polarized EM waves illuminate the RHMM waveguide array with varied rotation angle, nearly all the EM waves (~98%) will be converted into the cross-polarized EM waves [Figure S17].

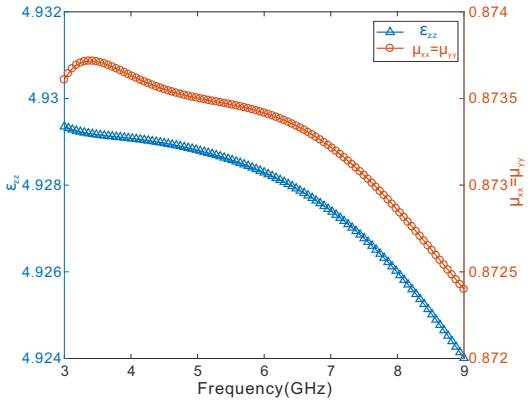

Figure S15. The effective permittivity, and permeability of the HMM consisting of alternating Cu/FR4 layers with t_m=0.068 mm, and t_d=0.47 mm.

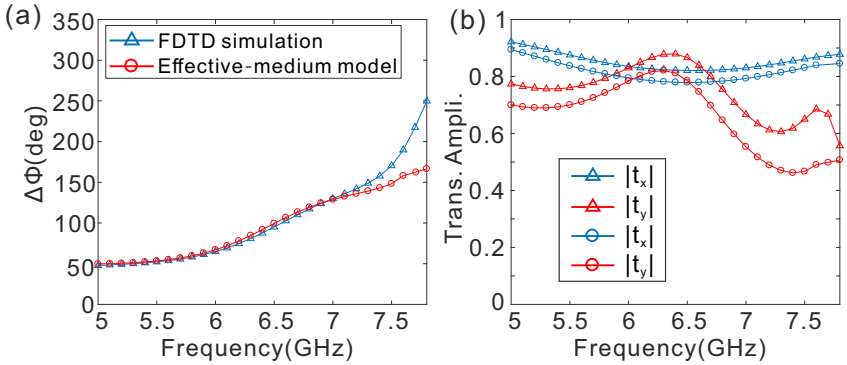

Figure S16. (a) The phase difference ($\Delta\varphi$) between x- and y-polarized EM waves with (W_x, W_y)=(6 mm, 9 mm). (b) Transmission amplitude for x-, and y-polarizations. The solid lines with triangular and circular symbols are retrieved by FDTD simulation, and effective-medium model, respectively. In the calculation, it is assumed that 35 pair of Cu/FR4 layers (t_m =0.068 mm, t_d=0.47 mm) are used to construct the RHMM waveguide array, which is placed on a 2mm-thickness FR4 substrate. The lattice constants in x-y plane are chosen as $P_x = P_y$=13 mm.

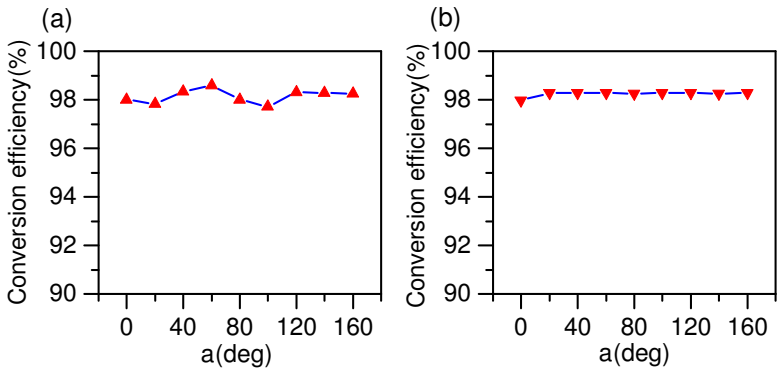

Figure S17. The simulated polarization conversion efficiency versus rotation angle, α, of the RHMM waveguide array, illuminated with a normal-incidence RCP (a) and LCP (b) plane wave at 7.6 GHz.

Note 12: Simulated and measured near-field electric field of the CP EM wave deflector

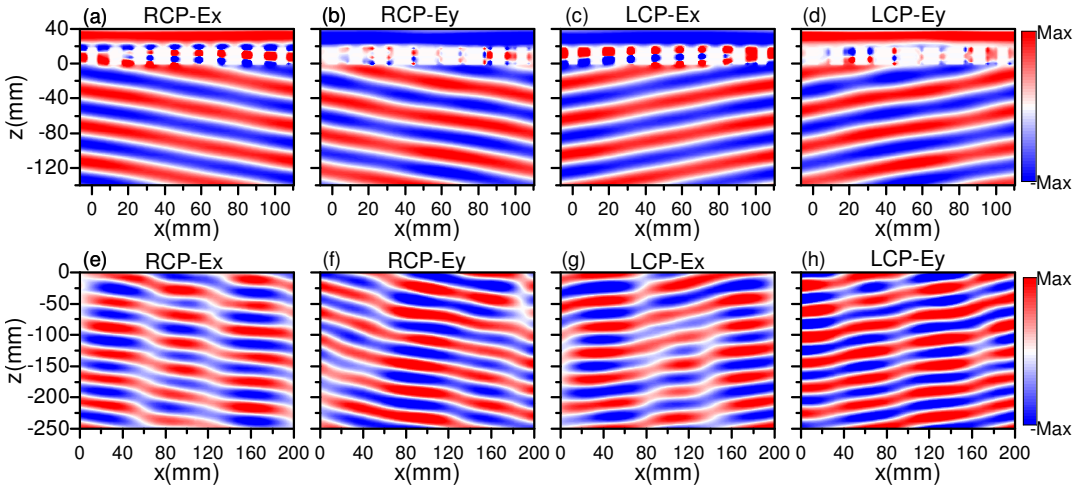

Figure S18. The simulated (a-d), and measured (e-h) electric field distributions of (E_x , E_y) with RCP (a, b, e, f), and LCP (c, d, g, h) plane wave of normal incidence, respectively.

Note 13: The diverging effect for the LCP incidence

As for the LCP incidence, the PB phase shift of the transmitted EM waves shows an opposite sign compared to the RCP incidence. Different from the focusing effect for the RCP incidence, the EM waves diverge in the output space for the LCP incidence [Figure S19].

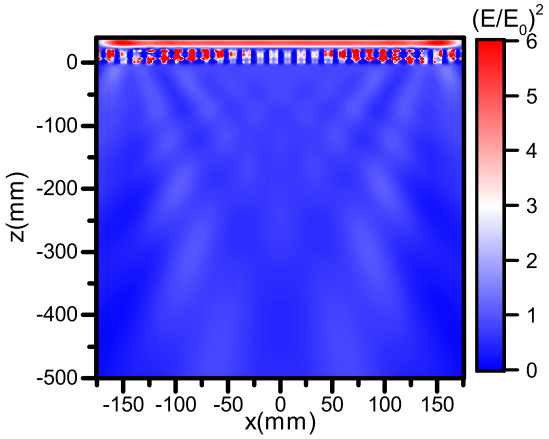

Figure S19. The simulated field intensity distribution in *x*-*z* plane, when the RHMM waveguide array is normally illuminated with the LCP at 7.6 GHz.

Note 14: The spectral property of the HMM beam deflectors

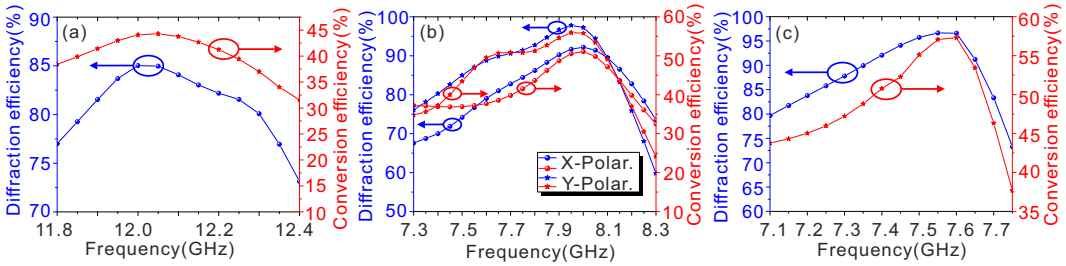

Figure S20. The simulated spectrum of diffraction and conversion efficiencies for (a) 1D-HMM, (b) SHMM, and (c) RHMM deflectors.

We have presented the simulated spectrum of diffraction and conversion efficiencies for the three beam deflectors [Figure S20]. The operation bandwidths (> 80% diffraction efficiency) are 0.4 GHz with the 1D-HMM [Figure S20a], 0.6 GHz for x-polarization, and 0.8 GHz for y-polarization with the SHMM [Figure S20b], and 0.6 GHz with the RHMM deflectors [Figure S20c], respectively.

Note 15: The diffraction/conversion efficiencies versus the incidence angle

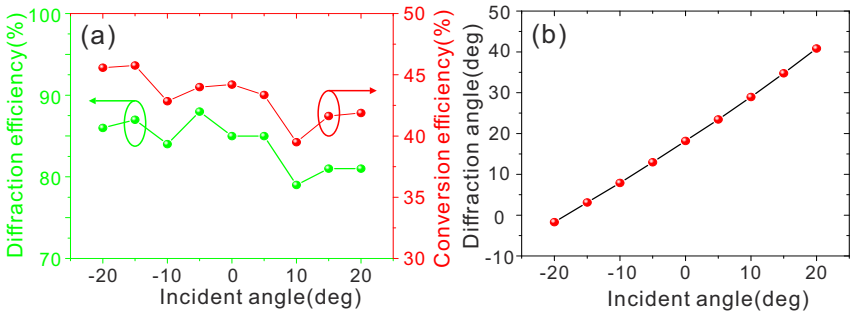

Figure S21. (a) The dependence of the diffraction/conversion efficiencies for the polarization-dependent beam deflector on the incidence angle. (b) The diffraction angle versus the incidence angle.

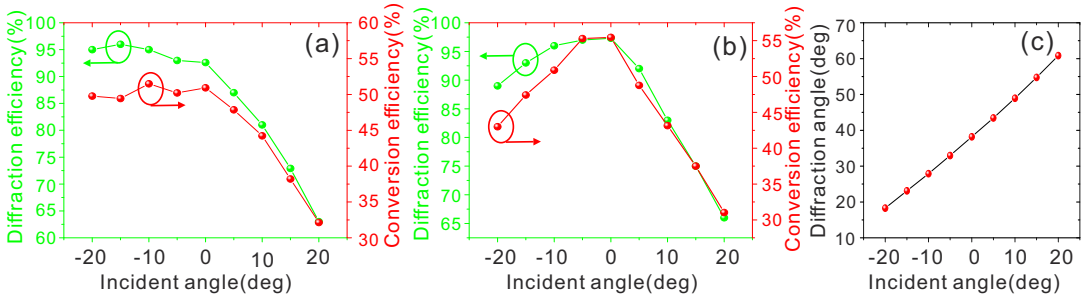

Figure S22. The dependence of the diffraction/conversion efficiencies for the polarization-independent beam deflector on the incidence angle with (a) x- and (b) y-polarized incidences, respectively. (c) The diffraction angle versus the incidence angle for x- (y-) polarized incidence.

We have calculated the diffraction/conversion efficiencies for the HMM beam deflectors in Figure S21-S23. For the linearly-polarized beam deflectors, the diffraction efficiency can reach above 80% for most angles if the incidence angle ranges from -20 to 20° [Figure S21-S22]. For the CPEM beam deflector, the diffraction efficiency can maintain >90% when the incidence angle is within the whole range of -20° to 20° for both of LCP and RCP incidences [Figure S23]. Overall, the HMM beam deflectors show rather robustness to the incidence angle, which is largely shifted to 20°.

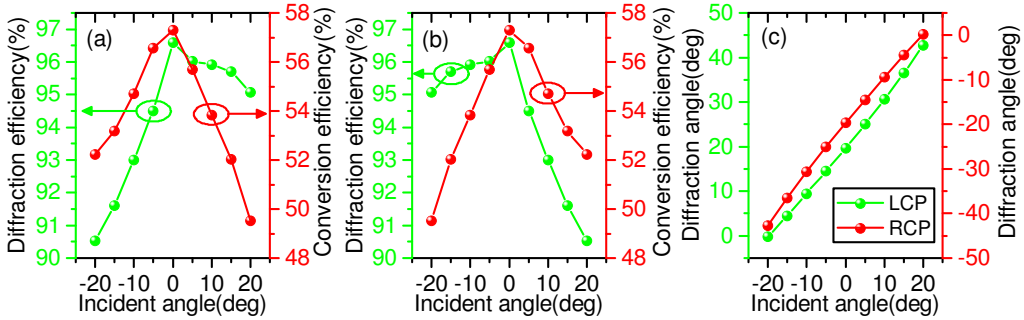

Figure S23. The dependence of the diffraction/conversion efficiencies for the HMM beam deflector on the incidence angle with (a) LCP and (b) RCP incidences, respectively. (c) The diffraction angles versus the incidence angle for LCP and RCP incidences, respectively.

Note 16: Comparison of the dispersion relations between a traditional plasmonic waveguide (array) and an HMM waveguide (array) in the optical spectral domain

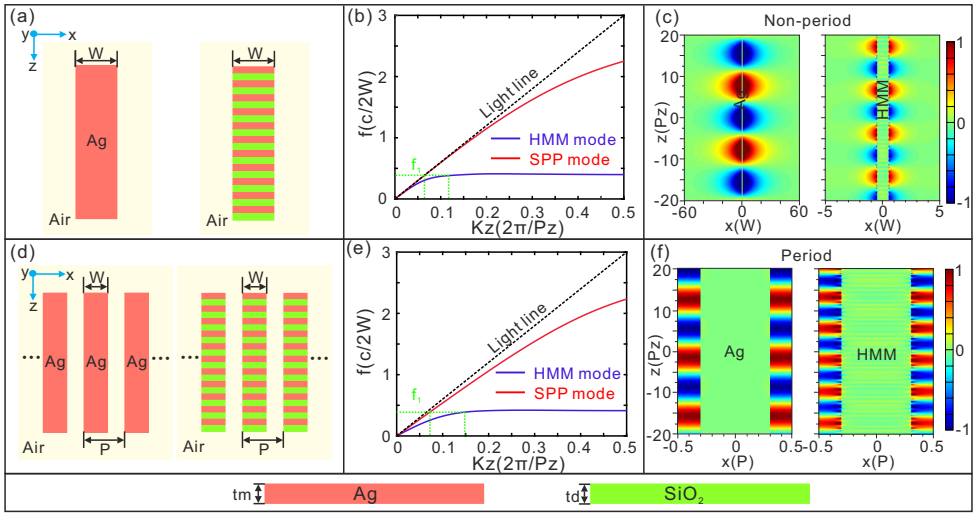

Figure S24. (a) The air/Ag/air (left panel) and air/HMM/air (right panel) waveguides. (b) The dispersion curves calculated for the two cases with the equal waveguide width of W =300 nm. Ag and SiO_2 (n_d=1.45) are taken as the metal and dielectric layer with t_m =50 nm, t_d =50 nm, and their dielectric constants are from the experimental data [A5]. (c) The electric field distributions of E_x of the surface bounded modes at 1550 nm for the two waveguides. (d) The air/Ag/air (left panel) and air/HMM/air (right panel) waveguide array. (e) The dispersion curves calculated for the two waveguide arrays with the equal period of P=500 nm, while the other geometrical parameters are the same as those used in (b). (f) The electric field distributions of E_x of the surface bounded modes at 1550 nm for the two waveguide arrays.

By scaling down the metal-dielectric multi-layers, the operating frequencies of the SSP mode with the HMM waveguide can be scaled from microwave to THz, to infrared, or even to visible domain. We show in Figure S24a-c that, the dispersion curve of the surface bound waves with the HMM waveguide has strong resemblance with a traditional metal stripe waveguide (air-metal-air). For simplicity, we only show the symmetric surface bounded waves, while high-order waveguide modes are not mentioned here. It is interesting to find that the dispersion curve for the surface bounded EM waves with the HMM waveguide deviates more from the light line, compared to that with air-metal-air waveguide of the same width. More interestingly, the asymptote of the dispersion curve with the HMM waveguide is mainly controlled by the geometry defining the multi-layers, while that for the case of air-metal-air waveguide is mainly determined by the metal material used. When the HMM waveguides are arranged in an array [Figure S24d-f], the coupling of the surface bounded waves between the adjacent HMM waveguides will significantly pull the dispersion curve further away from the

light line, showing the robust and flexible capability of tuning the phase delay of the transmitted EM waves.

Note 17: Design of the polarization-independent beam deflector at 1550 nm

Our polarization-independent wave shaping device can be generalized to high frequency region. Here we have designed beam deflectors and focusing lenses at the near-infrared frequency by using the SHMM waveguide array. By carefully selecting the sub-unit period of 500 nm, the transmission intensity and the phase shift at λ=1550 nm versus the SHMM waveguide width can be calculated [Figure S25]. The phase distributions cover 0-2π range with the SHMM height of 800 nm (~0.52λ).

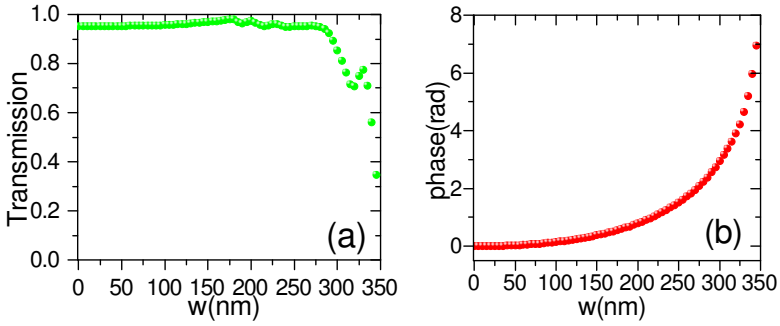

Figure S25. The dependence of the transmission intensity (a) and phase shift (b) on the width of SHMM waveguid, *W*, with the sub-unit period of 500 nm, when the working wavelength is at 1550 nm. The HMM is comprised of 8 pair of Ag/SiO_2 layers with t_m =50, and t_d =50 nm. The SHMM waveguide array sits on SiO_2 substrate.

We have designed a polarization-independent beam deflector with the lattice constant, *Lx*, of 3000 nm. When the SHMM waveguides are arranged in an array, the modal characteristics of each waveguide may be varied due to the change of the dielectric environment, which thus enables a slightly different efficiency for x- and y-polarized incidences. To make the designed beam deflector work without polarization dependence, we have optimized the widths along x- and y-directions. The optimized widths of the sub-units in each super-cell for the beam deflectors are shown in Table S1. The simulation results demonstrate that the SHMM waveguide array based on the optimized widths enables the beam deflecting with good polarization independence. The diffraction (conversion) efficiencies reach as high as 93%

(73%), and 92% (71%) for x- and y-polarized incidences, respectively [Figure S26b,d]. The conversion efficiencies here are much higher than those in the microwave regime, thanks to the lower reflection at the HMM-air interface in the infrared frequency region.

No. / Width	1	2	3	4	5	6
Wx(nm)	0	221	275	305	324	350
Wy(nm)	0	221	275	305	324	335

Table S1. The distributions of width within a super-cell for the designed polarization-independent beam deflector. The number of the sub-units used in a super-cell is 6.

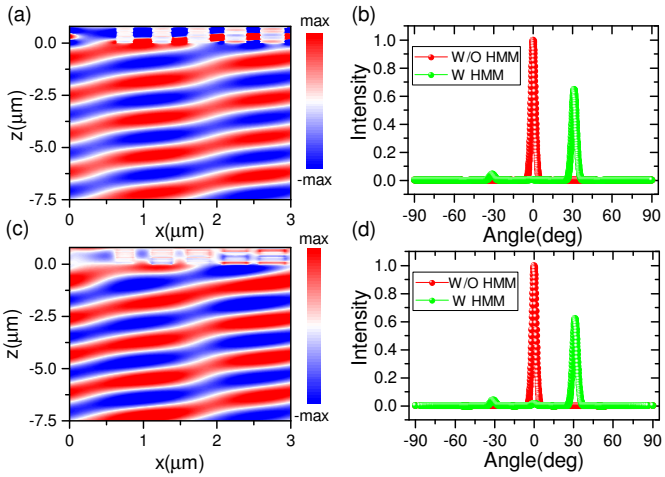

Figure S26. The simulated electric field distributions in *x-z* plane for x- (a), and y-polarized (c) incidences at 1550 nm. The simulated far-field intensity with and without the SHMM waveguides for x- (b), and y-polarized (d) incidences at 1550 nm. The distributions of the width of each sub-unit in a super-cell are shown in Table S1. All the other geometrical parameters are the same as those in Figure S25.

Note 18: Design of the polarization-independent focusing lens at 1550 nm

By further arranging the SHMM waveguide arrays to enable the phase distributions to abide by a hyperboloidal profile, a focusing lens can be designed at 1550 nm [Figure S27]. Here, the focal length for the focusing lens is fixed at 10 μm with the working wavelength of 1550 nm. With NA of 0.71, the field intensity enhancement in the focal plane can reach 9.6 and 15.7 for x-, and y-polarized incidences, respectively, and the evaluated FWHM of the focusing spots are about 0.72λ, and 0.59λ for x-, and y-polarized incidences, respectively, being highly diffraction-limited see Figure S27b,d.

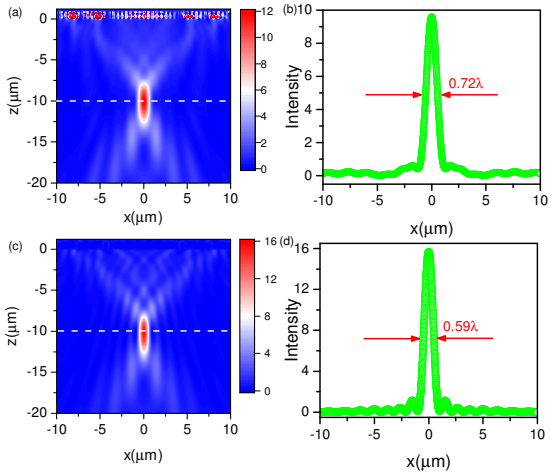

Figure S27. The simulated electric field intensity in *x*-*z* plane for x- (a), and y-polarized (c) incidences, respectively, with the working wavelength of 1550 nm. (b, d) The simulated normalized electric field intensity profile along the white dashed line in (a), and (c), respectively. The focusing length is set to be 10 μm with NA of 0.71. All the other geometrical parameters are the same as those in Figure S25.

Note 19: Design of the CP deflector at 1550 nm

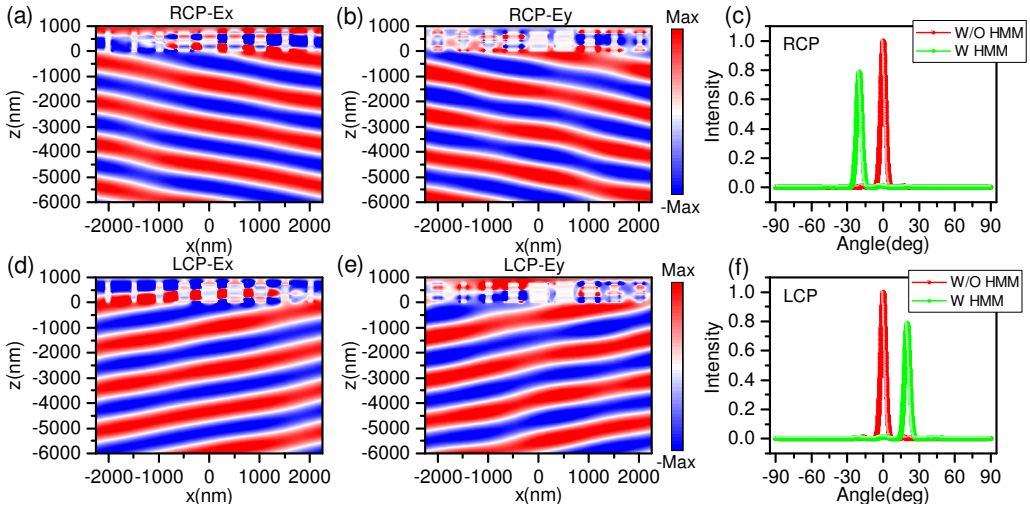

Figure S28. The simulated electric field distribution for RCP [(a) *Ex*-component, and (b) *Ey*-component], and LCP [(d) *Ex*-component, and (e) *Ey*-component] incidences at 1550 nm. The simulated far-field electric field intensity profile with and without the RHMM waveguides for RCP (c), and LCP (f) incidences at 1550 nm. The HMM is comprised of 8 pair of Ag/SiO_2 layers with t_m =50 nm, and t_d =50 nm. The HMM waveguide arrays sit on SiO_2 substrate. The other geometrical parameters are set to be $P_x = P_y$ =500 nm, W_x=129 nm, and W_y=344 nm.

Here, we design a deflector and focusing lens at the near-infrared frequency based on the PB phase. The design approach is analogous to that presented in the main text. We first design a half-wave plate at 1550 nm to ensure a high polarization conversion efficiency. By appropriately choosing the geometrical parameters [see the caption of Figure S28 for the detailed parameters], the simulated transmission amplitude for x-, and y-polarized incidences

are $|t_x|$ =0.99, $|t_y|$ =0.82, respectively, and the phase difference between the x-, and y-polarized incidences is 1.04π. The simulation results conducted by FDTD further reveal that the designed RHMM waveguide with successive rotation angle of π/9 enables the beam deflection, both for the RCP, and LCP incidences. The near-field distributions from Figure S28a,b,d,e indicate an apparent light deflection. The diffraction efficiency and conversion efficiency of light deflection at 1550 nm are 95.1%, and 77.9% both for the RCP, and LCP incidences [Figure S28c,f].

Note 20: Design of the CP focusing lens at 1550 nm

By further arranging the RHMM waveguide arrays to enable the phase distributions to follow a hyperboloidal profile described by Equation 5 in the main text, a planar focusing lens working for the CP light waves can be designed at 1550 nm. The focusing lens presents the dual-functionality that depends on the CP states of incident light. Light with RCP incidence is focused into a diffraction-limited spot with FWHM of 0.62λ and field intensity enhancement 15-fold larger than the incident light [NA=0.71, Figure S29a, c]. The actual focusing length of 9.1 μm is shorter than the designed one of 10 μm, due to the finite-size effect. By contrast, light with the LCP incidence undergoes a divergence in the output space [Figure S29b].

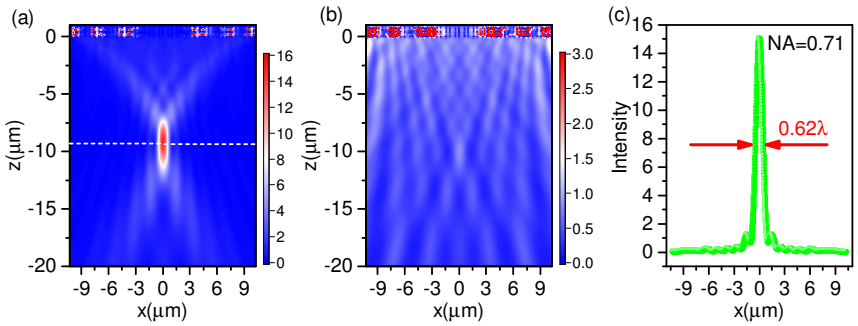

Figure S29. (a) The simulated electric field intensity in *x-z* plane for RCP (a), and LCP (b) incidences, respectively, with the working wavelength of 1550 nm. (c) The simulated normalized electric field intensity profile along the white dashed line in (a). The focusing length is set to be 10μm with NA of 0.71. All the other geometrical parameters are the same as those in Figure S28.

Note 21: Fabrication method of the HMM metasurface at short wavelengths

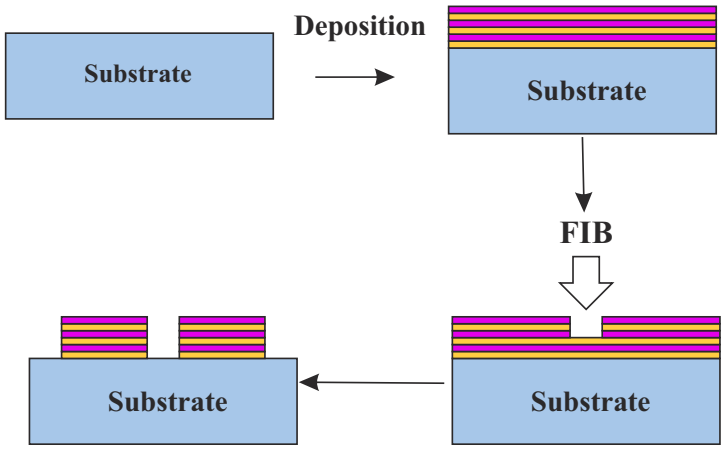

Figure S30. The schematic of the fabricating process of the HMM metasurface.

As shown in Figure S30, two steps should be taken to prepare the HMM metasurface at short wavelengths. First, sequential deposition of SiO_2/Ag multi-layer on a glass substrate can be realized by using sputtering technique or electron beam evaporation technique. A focused-ion-beam milling is then followed to form the HMM waveguide array. This experimental fabrication process has been extensively used for fabricating the HMM structures [A6-A10].

Note 22: Fabrication tolerance of the HMM waveguide array in the infrared region.

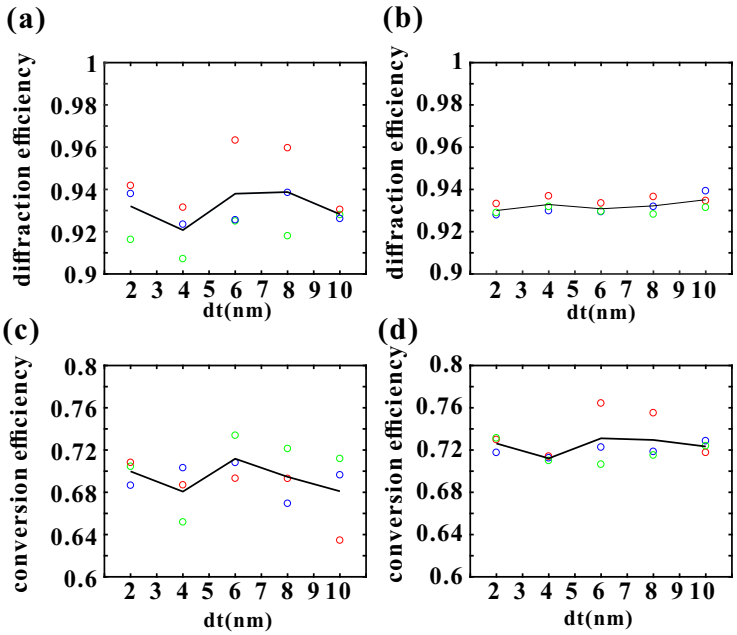

Figure S31. The diffraction efficiency (a, b) and conversion efficiency (c, d) versus the thickness error, dt, for x- (a, c) and y- (b, d) polarized incidences. The hollow circles are the simulated results, while the black solid lines represent the average values of the simulated results.

Note 23: Design of the polarization-independent beam deflector with tapered SHMM waveguide at 1550 nm

Here, we consider to build a beam deflector by using the tapered SHMM waveguide array with the slant angle α of of 5° [Figure S32 (a)]. As shown in Figure S32 and Figure S25 in Note 17, the phase and intensity transmission properties of tapered SHMM waveguides with a slant angle of 5° [Figure S32] are somewhat different from the one with zero slant angle [Figure S25]. We can see that the phase coverage of full 2π range can still be obtained when the width of the HMM waveguide, *w*, ranges from 0 to 320 nm, but the intensity tranmission is relatively smaller.

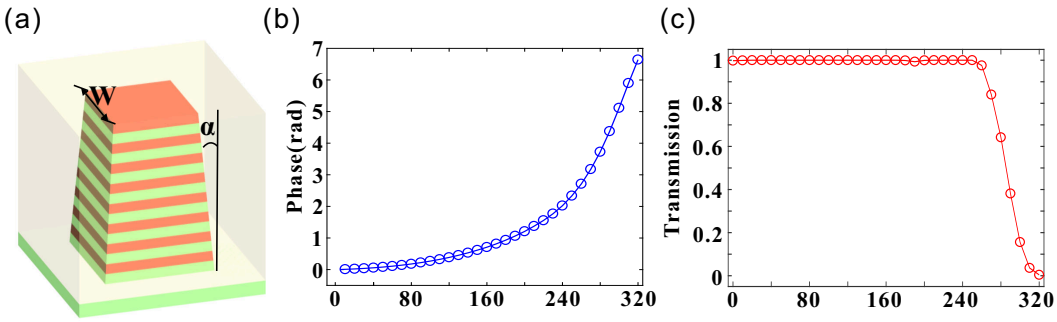

Figure 32. (a) Schematic of a unit cell of SHMM waveguide unit with an oblique side wall. The transmission phase (b) and intensity transmission (c) versus, *w*, for x- and y- polarized incidences.

No. / Width	1	2	3	4	5	6
w(nm)	0	189	242	269	287	306

Table S2. The distributions of width within a super-cell for the designed polarization-independent beam deflector. The number of the sub-units used in a super-cell is 6.

Further, when the tapered SHMM waveguides are arranged in an array as the widths of the sub-units within a super-cell for the beam deflectors are shown in Table S2. The simulation results demonstrate that the tapered SHMM waveguide array enables the beam deflecting with good polarization independence. The diffraction (conversion) efficiencies can keep as high as 93% (60%), and 96% (57%) for x- and y-polarized incidences, respectively [Figure S33]. The diffraction/conversion efficiencies are slightly smaller than those with vertical side walls.

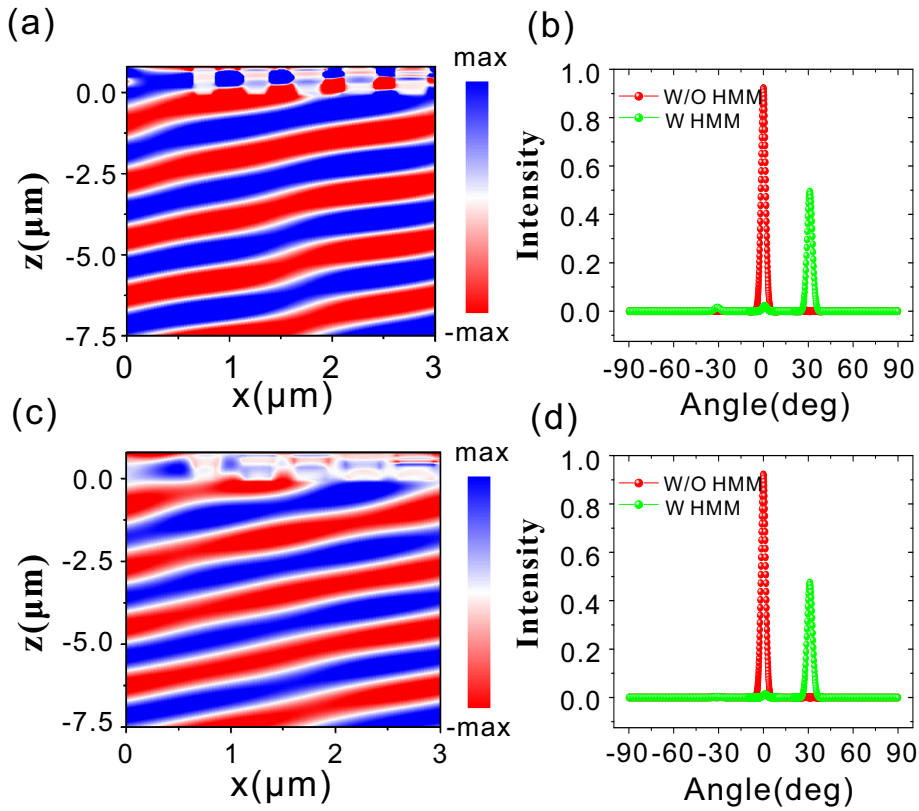

Figure S33. The simulated electric field distributions in *x-z* plane for x- (a), and y-polarized (c) incidences by using the tapered SHMM waveguide array with the slant angle α of 5° at 1550 nm. The simulated far-field intensity with and without the tapered SHMM waveguides for x- (b), and y-polarized (d) incidences. The distributions of the width of each sub-unit within a super-cell are shown in Table S2. All the other geometrical parameters are the same as those in Figure S25 in Note 17.

References

[A1] L. Li, J. Mod. Opt. **1993**, 40, 553.
[A2] M. Moharam, T. Gaylord, E. B. Grann, and D. A. Pommet, J. Opt. Soc. Am. A **1995**, 12, 1068.
[A3] A. W. Snyder, J. D. Love, *Optical Waveguide Theory*, Kluwer, London, **1983**.
[A4] N. Yu, P. Genevet, M. A. Kats, F. Aieta, J.-P. Tetienne, F. Capasso, and Z. Gaburro, Science **2011**, 334, 333.
[A5] E. Palik, *Handbook of Optical Constants of Solids.* New York, NY, USA: Academic, **1991**.
[A6] D. Lu, J. J. Kan, E. E. Fullerton, and Z. Liu, Nat. Nanotech. **2014**, 9, 48.
[A7] J. Valentine, S. Zhang, T. Zentgraf, E. Ulin-Avila, D. A. Genov, G. Bartal, and X. Zhang, Nature **2008**, 455, 376.
[A8] S. S. Kruk, Z. J. Wong, E. Pshenay-Severin, K. O'Brien, D. N. Neshev, Y. S. Kivshar, and X. Zhang, Nat. Commun. **2016**, **7**, 11329.
[A9] D. Ji, H. Song, X. Zeng, H. Hu, K. Liu, N. Zhang, and Q. Gan, Sci. Rep. **2014**, 4, 4498.
[A10] D. Lu, H. Qian, K. Wang, H. Shen, F. Wei, Y. Jiang, E. E. Fullerton, P. K. L. Yu, and Z. Liu, Adv. Mater. **2018**, 30, 1706411.